The Dependency of Compressive Response of Epoxy Syntactic Foam on the Strain Rate and Temperature under Rigid Confinement

Longhui Zhang[1*], David Townsend[1], Nik Petrinic[1], Antonio Pellegrino[1]

[1] Department of Engineering Science, University of Oxford, Parks Road, Oxford, OX1 3PJ, U.K.

[*]Corresponding author: longhui.zhang@eng.ox.ac.uk

Abstract:

Syntactic foam is being increasingly conceived for aero engine applications to enhance overall structural reliability under impact loading. Systematic compressive tests without and with lateral confinement are carried out to investigate the deformation and failure of an epoxy syntactic foam (ESF) at quasi-static 0.01 /s, medium rate 10-100 /s and high strain rates 500-1100 /s at gradually increasing temperatures from room temperature 25 ℃ to 150 ℃. The stress–strain response and the corresponding deformation process, complemented by Digital Image Correlation (DIC) technique, were monitored to reveal the dynamic deformation and strain localization of the foam. The elastic-brittle behavior without confinement at high strain rates can be suppressed by the lateral confinement and by elevated temperatures above 100 ℃. The lateral confinement slightly increases yield stress and significantly improves the energy absorption of ESF. Both confined yield stress and energy absorption evolve nonlinearly with strain rate and temperature. The strain hardening in the elastic-plastic behavior of ESF under confinement is strain rate independent, compared to its modest temperature dependency. A nonlinear phenomenological model is found to be able to describe the unconfined and confined responses of ESF and its temperature-strain rate equivalence, and reveal the competition between strain hardening and strain softening which is influenced by temperature.

Keywords: Syntactic Foam, Strain rate, Temperature, Confined compression, Hopkinson bar, Dynamic Shear Localization

1. Introduction

Polymeric syntactic foam, which consists of randomly distributed low density hollow particles in the polymeric matrix and owns high strength to weight ratio and good impact resistance, is being increasingly used in automobile and aerospace industries [1-5]. The syntactic foams can be mixed-use with plastic and metal components, or as a core material in sandwiched structures, in order to improve the load bearing capability of the integral structures. With the development of the new material and composites, it is necessary to understand the mechanical behavior of syntactic foam under various loading conditions.

The mechanical property of syntactic foam has attracted lots of interest in the past two decades [6, 7], i.e. the influence of microstructure on the material property [8], the functional gradient foam [9], and the fracture mechanisms resulting from the external loading [10]. The syntactic foam under quasi-static compressive conditions has been extensively reported, which usually shows three deformation stages [4] including the elastic behavior, plastic response with strain hardening or softening, and densification with rapidly increasing stress. It is also important to investigate the dynamic behavior of syntactic foams under high-speed conditions. Song et al. [11] studied the dynamic uniaxial compressive behavior of an epoxy syntactic foam using a modified SHPB and obtained the uniaxial stress-strain relationship over different strain rate regions. Ghatu et al. [12] investigated the uniaxial compressive behavior of several polymeric foams under quasi-static and dynamic loading conditions. It is found that the low density foam fractured in a brittle manner while the high density foam showed dominated shear failure mode regardless of the loading conditions. Rittel [13] conducted ballistic tests to identify the failure modes of the foam using a gas gun to fire cylindrical syntactic foam projectiles at different velocities towards the metallic panels. Recently, Li et al. [14] studied the behavior of a glass microballoon epoxy syntactic foam from low to high strain rates by combining the experiment and finite element simulation to reveal the underlying deformation and fracture mechanisms. Arezoo et al. [15, 16] performed comprehensive experimental work to investigate the sensitivity of the uniaxial compressive response of a series of Rohacell foams at

various strain rates and temperatures ranging from 203 to 473 K. The temperature sensitivity of the foams was corrected to strain rate dependent elasto-plastic response via time–temperature superposition. DIC is a popular non-contact technique for the measurement of deformation and strain fields in the past decades [17, 18]. The DIC analysis would provide more information on the deformation process of syntactic foam, compared to the sole results of global stress-strain relationship by assuming uniform strain and stress fields, as indicated by Pellegrino et al. [18] and Liu et al. [19]. *The monitoring of dynamic deformation and failure process of syntactic foam with DIC under different loading conditions are less reported, which would be important for the understanding of the strain rate dependent behavior.*

Considering the actual response of syntactic foam in service, the direct use of uniaxial compressive data for real engineering applications needs to be addressed carefully. Song et al. [20] compared the elastic-brittle compressive behavior of an epoxy syntactic foam without confinement and the elastic-plastic compressive behavior with lateral confinement at low and high strain rates. Ghatu et al. [21] investigated the crushability behavior of epoxy polymeric foam in rigid confinement under quasi-static and high strain rate conditions, and compared the rate sensitivity of yield stress without confinement and with lateral confinement. Recently, Kully [22] performed the dynamic confined compression tests for Eco-Core and other core foams to determine the corresponding stress-strain relationship and the energy absorptions under multiaxial stress state.

The confinement is regarded to play an important role in increasing the deformability of syntactic foams. In aerospace industry, syntactic foam is being increasingly employed in fan containment assembly for a jet engine [23-25], in order to improve the toughness to effectively prevent penetration of the external bird strikes and the released fan blade and reduce the noise generated by the high-speed rotating engine. *Systemic accurate mechanical characterization of the unconfined and confined syntactic foam, across a wider range of strain rates than just quasi-static and high strain rates two regions, is compulsory for the effective design of the aircraft structures made from the foam materials.* Meanwhile, although not operated in ultra

high temperature like turbine combustor, the fan containment system in service undergoes various temperature conditions. *However, the temperature sensitivity on the syntactic foam without confinement and with lateral confinement is also less investigated.*

Therefore, the present paper studies the unconfined and confined compressive behavior of an epoxy syntactic foam (ESF), with the assistance of DIC technique [18, 26] across a wide range of strain rates and temperatures. The ESF conceived for the application in jet engine containment, jointly with lightweight titanium alloys [27, 28] as an integral impact resistant system, would improve the load bearing and energy absorption capabilities during impact events such as bird strike and fan blade off. The monitoring of dynamic deformation of ESF using DIC under different conditions will provide a better understanding of the strain rate dependent behavior and the failure mode transitions of ESF. Likewise, the influence of strain rate and temperature on confined constitutive response and the corresponding energy absorption, which is rarely reported in the literature, is investigated in the present work. The microstructural characterization is also conducted to obtain further insight into the unconfined and confined macro mechanical behavior. The material, specimens and experimental techniques are introduced in Section 2. The next two sections present the experimental results and the constitutive modelling analysis, followed by the discussion in Section 5 and the conclusion in Section 6.

2. Experimental Protocol

2.1 Material and specimens

The cylindrical specimens with 5mm diameter and 5mm length were prepared from an as received ESF rod. This supplied ESF, which is made of epoxy matrix containing amorphous silicate-based glass microballons, owns a low density of 715 kg/m^3 and provides a low thermal conductivity and cost-effective characteristics. The relevant mechanical and physical properties are listed in Table 1.

Property	Value
Thermal conductivity	0.11 W/m•K
Specific heat capacity	1.6 kJ/(kg ℃)
Coefficient of Thermal Expansion	39.6 x 10^{-6} m/m/ ℃
Flexural Toughness	18.6 kPa
Sound wave speed	2151 m/s

Table 1. Material properties of the investigated ESF

Fig.1 presents the initial (as received) microstructure consisting of glass microballons in epoxy matrix. The volume fraction of the glass spheres (defined as the ratio of the volume occupied by the balloons and the total volume) from X-Ray CT scan analysis is approximately 0.5. The microballons in epoxy matrix have an average diameter of 42 um with standard deviation of 27 um and an average wall thickness of about 1.10 μm. Fig.2 shows the glass transition temperature of 123 ℃ for the ESF, which was measured from Differential Scanning Calorimetry (DSC) by using TA Instruments DSC Q2000.

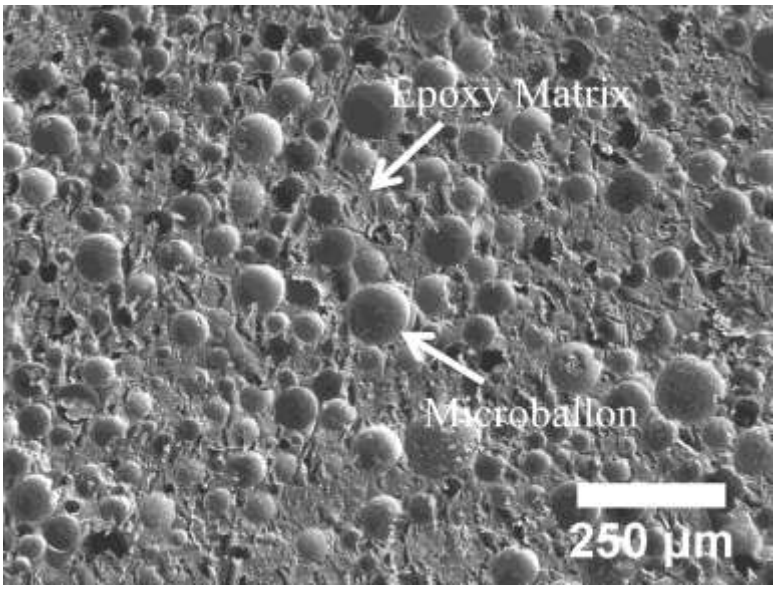

Fig.1 Scanning electron micrograph of initial microstructure of the as received epoxy syntactic foam

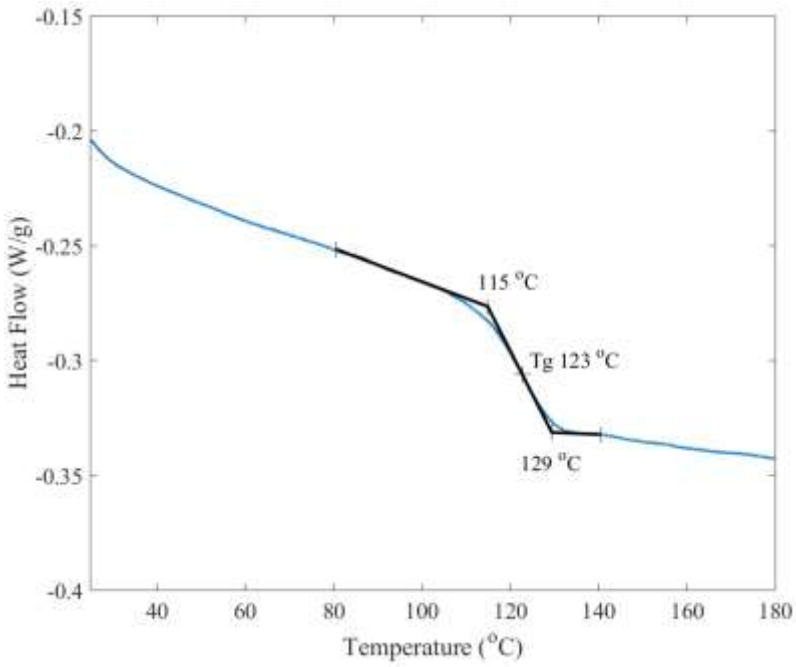

Fig.2 Heat flow as a function of temperature from DSC measurement for epoxy syntactic foam

A tube with 3 mm wall thickness and 5 mm internal diameter was manufactured from Ti6Al4V alloy to apply the rigid confinement. Fig.3 shows the assembly, with a 2.5 mm thick adapter also made from Ti6Al4V alloy on top of the confined specimen to apply the compressive loading. The syntactic foam, lubricated by grease, can be

inserted into the sleeve with hand pressure. It is assumed no friction between sleeve and foam in the present investigation.

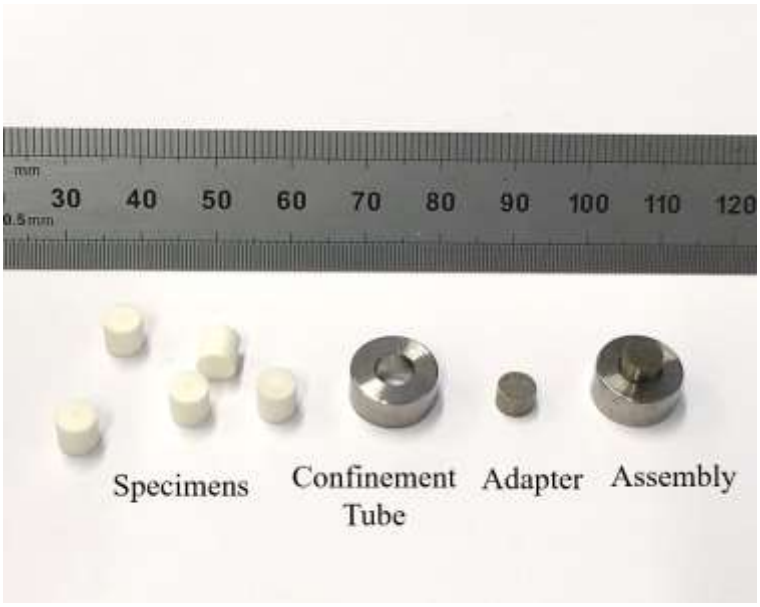

Fig.3 Images of the specimens and the confinement assembly

2.2 Experimental setup

2.2.1 Quasi-static testing

A Zwick Z50 screw driven machine was used for the quasi-static compression tests. The deformation of the specimen was recorded by an IDS UEye USB 3.0 Camera[1] system with a resolution of 2456x2054 pixels at a frame rate of 1 fps. The load platen was programmed to move at a constant speed corresponding to engineering strain rate 0.01 /s in the displacement control mode. Two tapes with speckle patterns were attached on the load platen to measure the displacement of specimen, with the assistance of commercial DIC software LaVision Davis[2] to obtain the macro engineering strain of the specimen.

[1] IDS Imaging Development Systems GmbH, Dimbacher Str. 6-8, 74182 Obersulm, Germany

[2] LaVisionUK Ltd, 2 Minton Place Victoria Road, Bicester OX26 6QB, United Kingdom

2.2.2 Medium rate testing

A hydraulic Instron machine 8854 was used to perform the medium rate compression tests. The deformation process was recorded by a Photron camera with a resolution of 256x768 pixels at a frame rate of 10,000 fps. The machine is controlled by applying the load under displacement control which corresponds to at engineering strain rates of 10 /s-100 /s to compressive the specimen.

2.2.3High strain rate testing

The experiments at high strain rate were conducted on a bespoke split Hopkinson compression bar [29, 30] synchronized with a high-speed Kirana camera, as shown schematically in Fig.4. The images with 924x748 pixels resolution were recorded by a Tamron SP60mm Macro lens at framing rates from 0.5-1x10^5 fps and shutter speed 5 us. The incident and transmitted bars are made of Ti6Al4V alloy, with 16mm diameter and 2.7m length for both two bars. A 2.5 m length striker bar is also made of Ti6Al4V alloy. Elevated temperature tests at 65 ℃, 100 ℃, 125 ℃ and 150 ℃ were carried out by using an environmental chamber equipped on the Hopkinson bar, in order to evaluate the temperature effect on the response of syntactic foam. An EPDM rubber with 0.7 mm thickness was placed at the impact end of incident bar as a pulse shaper. Grease was used for the lubrication between the specimen and the end of the bars. Three strain gauges were attached on the bars. Specifically, gauge 1 and 2 were for the measurements of incident (and reflected) wave signals on the incident bar, while gauge 3 was to measure the transmitted signal on the output bar. The boundary velocities and forces of the specimen are calculated by an in-house developed algorithm to separate the incident and reflected waves in the incident bar. The amplitude of propagating wave histories is determined by the D'Alambert's solution of wave equations, which can be found in Refs. [30, 31]. The stress and strain of the specimen are determined by the classical Hopkinson bar analysis. A typical incident and transmitted pulse are shown in Fig.5.

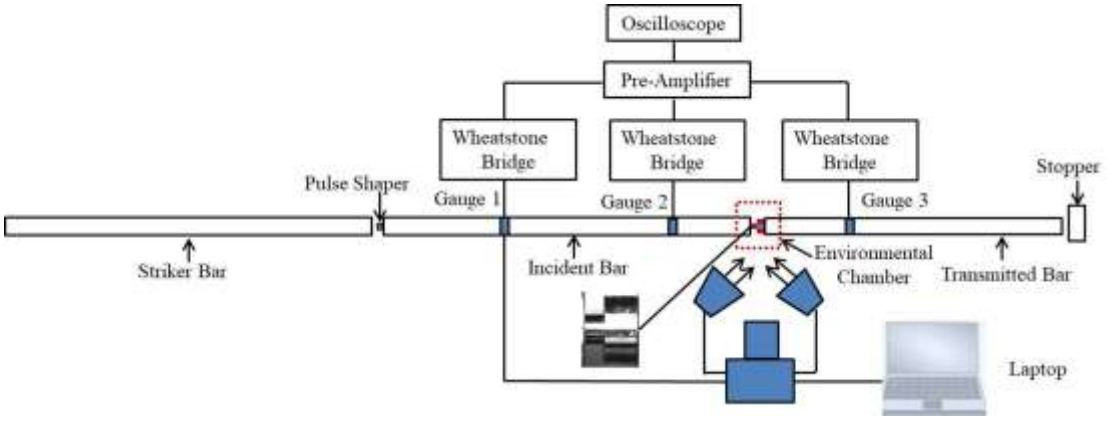

Fig.4. Schematic of Hopkinson bar system for high rate confined compression test

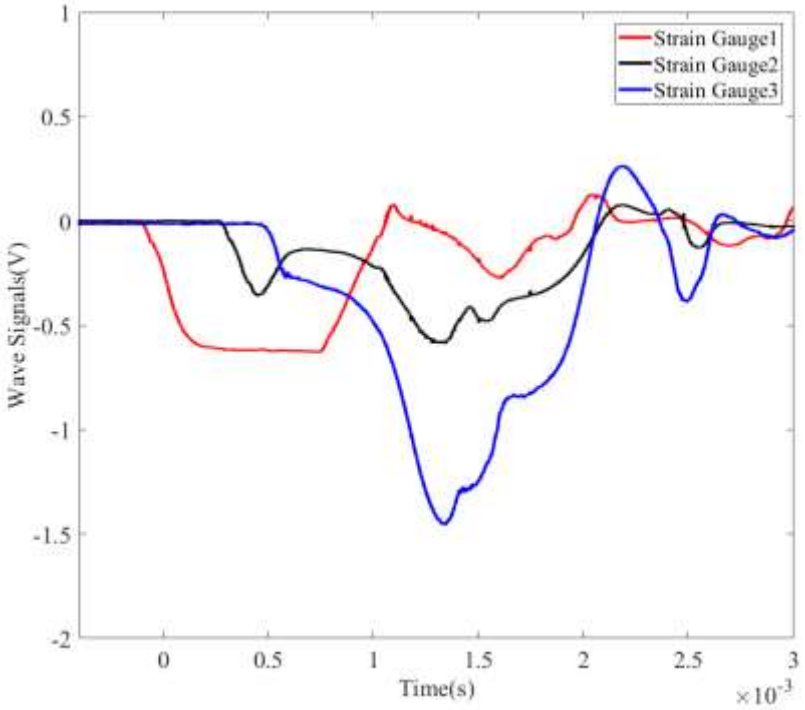

Fig.5 Typical raw strain gauge signals for a test at high strain rate of 720 /s and room temperature under confinement.

3. Experimental Results

3.1 Quasi-static and Medium rate Experimental Results

Fig.6 shows the unconfined and confined engineering stress-strain relationship at a nominal strain rate of 0.01 /s. In the present work, a point that diversifies from the linear behavior in the stress-strain relationship is defined as the yield stress of confined ESF, as can be seen in Fig.7. The peak stress is identified as the yield stress for unconfined ESF. Here, a method proposed by Li et al. [32, 33], based on the maximum energy absorption efficiency $\eta=\frac{1}{\sigma(\varepsilon)}\int_0^{\varepsilon}\sigma(\varepsilon)\,d\varepsilon$, is employed to identify the densification strain and the following densification stage. The energy density, which is the area under the stress-strain curve up to the densification strain, is calculated to evaluate the energy absorption capacity of ESF, as indicated by Goel et al. [34]. After yielding at about 52 MPa in the elastic stage, the stress without confinement decreases gradually and thereafter increases rapidly at densification strain of about 0.57. The confined stress-strain relationship shows a different response compared to that without confinement. Specifically, beyond the yield stress of approximately 53 MPa, the strain hardening stage is apparent, and the stress increases rapidly beyond a densification strain of 0.39. The average energy density up to densification strain for confined ESF is 33 J/m^3. This is higher than the energy density of 25 J/m^3 for ESF without confinement.

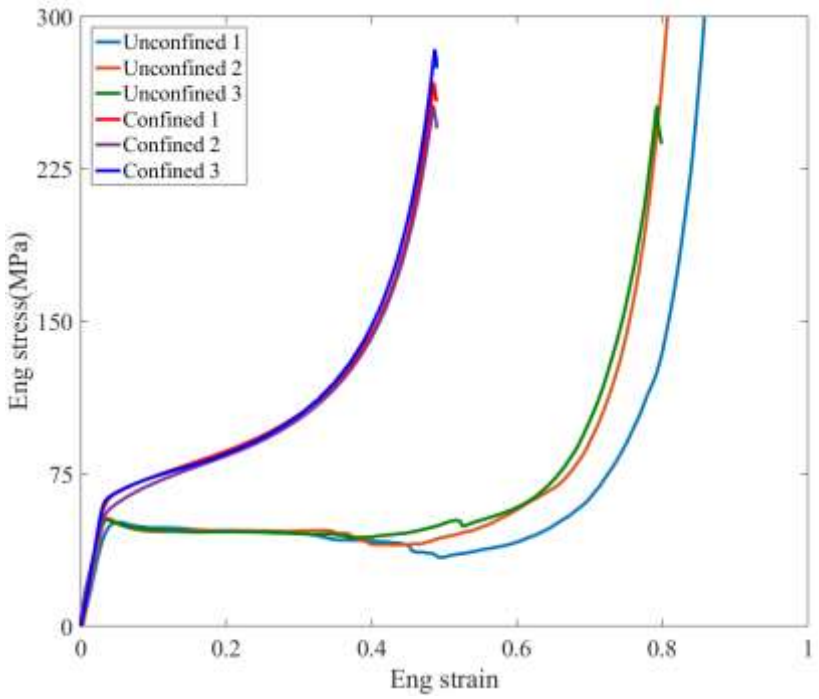

Fig.6 Quasi-static engineering stress-strain relationship without and with confinement

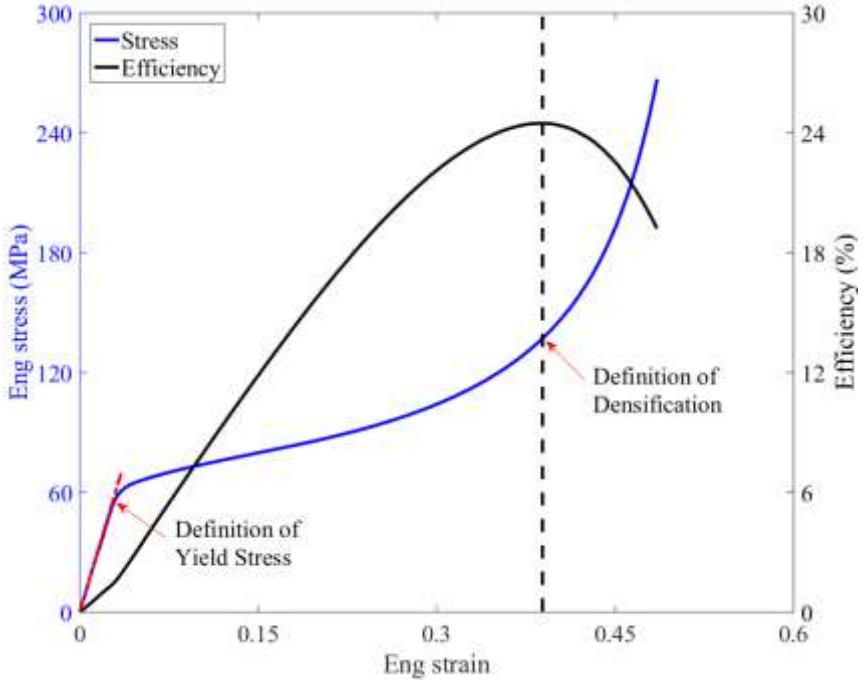

Fig.7 Definition of yield stress and densification strain for the confined stress-strain relationship. Note the elastic-plastic response of the behavior with confinement.

The unconfined and confined engineering stress-strain relationships at nominal strain rates of 10-100 /s are compared in Fig.8. The specimens were only loaded to

engineering strain less than 0.75, in order to protect the compression load cell at high loading speed of 50-500 mm/s on the Instron machine. The force measurement from the sensor fixed on the base of the Instron machine shows oscillations because of the elastic response and the inertia of the measurement system. The difference between the specimen without confinement and with rigid confinement is observed. The confined yield stress about 72 MPa is higher than 70 MPa without confinement. The confined stress-strain relationship shows significant strain hardening and dramatically increasing stress at a densification strain of 0.37. The unconfined stress-strain relationship shows strain softening followed by a slight increase in stress at a densification strain of 0.57. The average energy density up to densification strain for confined ESF is 36 J/m^3 at medium rate of 10-50 /s, which is higher than the energy density of 24 J/m^3 for unconfined ESF.

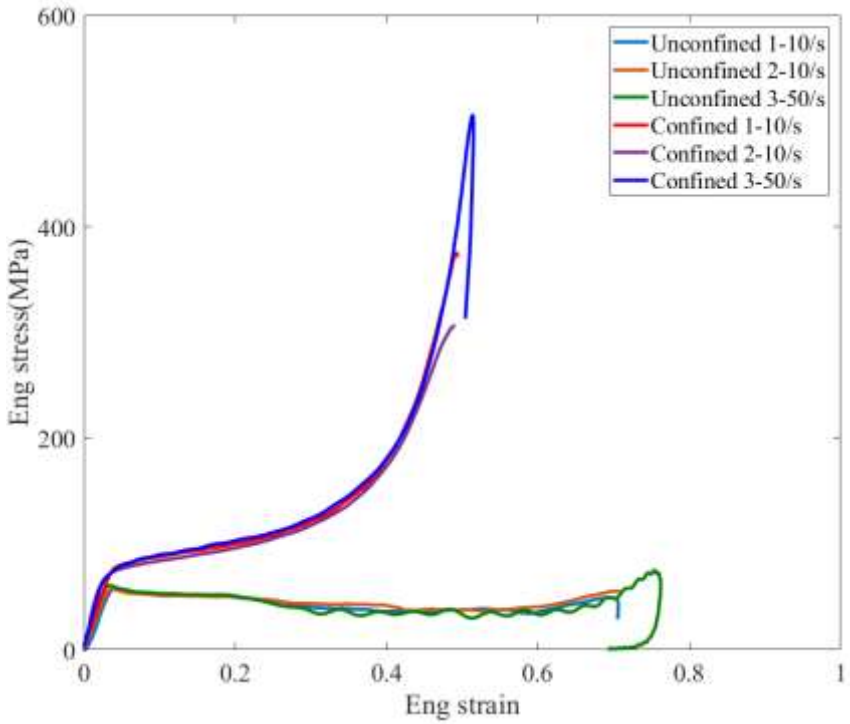

Fig.8 Engineering stress-strain relationship without and with confinement at nominal strain rate of 10-50/s

3.2 High Strain Rate Experimental Results

High strain rate tests were performed at nominal strain rates from 500 /s-1100 /s on the Hopkinson bar system. The dynamic force equilibrium condition is required for a valid Hopkinson bar experiment. Fig.9 compares the typical input force and output force for a dynamic confined test, in which the good force equilibrum is achieved. The specimen was fully loaded with the duration 1.1 ms on the bespoke Hopkinson bar system, followed by the unloading after the time about 1.95 ms (arrowed).

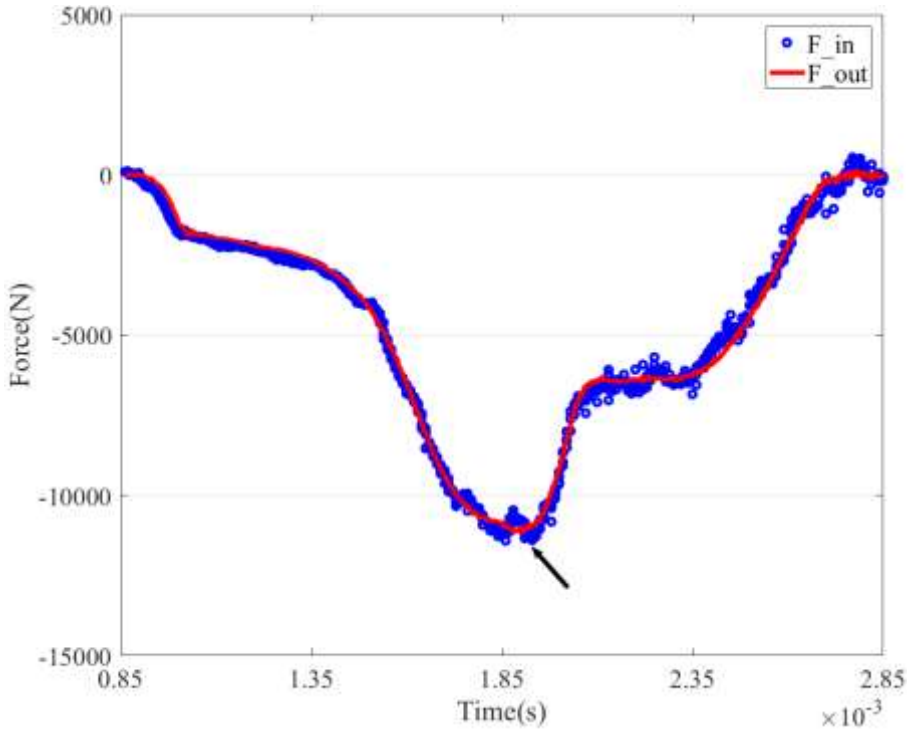

Fig.9 Dynamic force equilibrium in a confined test at high strain rate of 720/s.

The engineering stress-strain relationship without confinement at high strain rates is compared to the confined stress-strain relationship in Fig.10. The first observation is the unconfined stress decreases rapidly after the yield stress of 70 MPa, and the ESF gradually loses the load bearing capacity. However, the confined stress shows a significant strain hardening with a further dramatic increase at densification strain of 0.36. The yield stress under confinement is about 72 MPa, which is slightly higher than that without confinement.

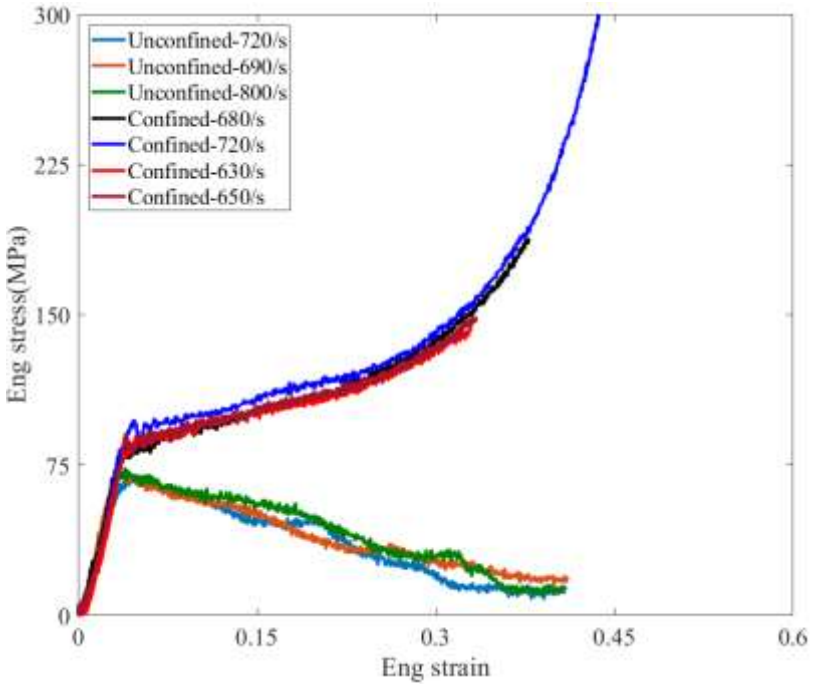

Fig.10 Engineering stress-strain relationship without and with confinement at high strain rates and room temperature

Fig.11 shows the engineering stress-strain relationship of the unconfined specimens from quasi-static to high strain rates. The yield stress increases from 52 MPa at 0.01 /s, 58 MPa at 10 /s to 70 MPa at 800 /s. The decrease of stress after the yield stress also shows apparent strain rate dependency. The ESF deforming at high strain rates drops from 70 MPa to 10 MPa at the strain of 0.3, while at medium rates the stress decrease to the values above 30 MPa. The densification stage with increasing stress can still be seen at low strain rates and medium rates, however, the real densification stage of elastic-brittle behavior at high strain rate is absent.

Considering the confined engineering stress-strain relationship from low to high rates, one can find that the strain rate effect on the yield stress is apparent, which increases from 52 MPa at 0.01/s, 59 MPa at 10 /s to 74 MPa at 720 /s. All confined stress-strain relationships present elastic-plastic characteristics with significant strain hardening, and the hardening capacity appears not to be apparently strain rate dependent.

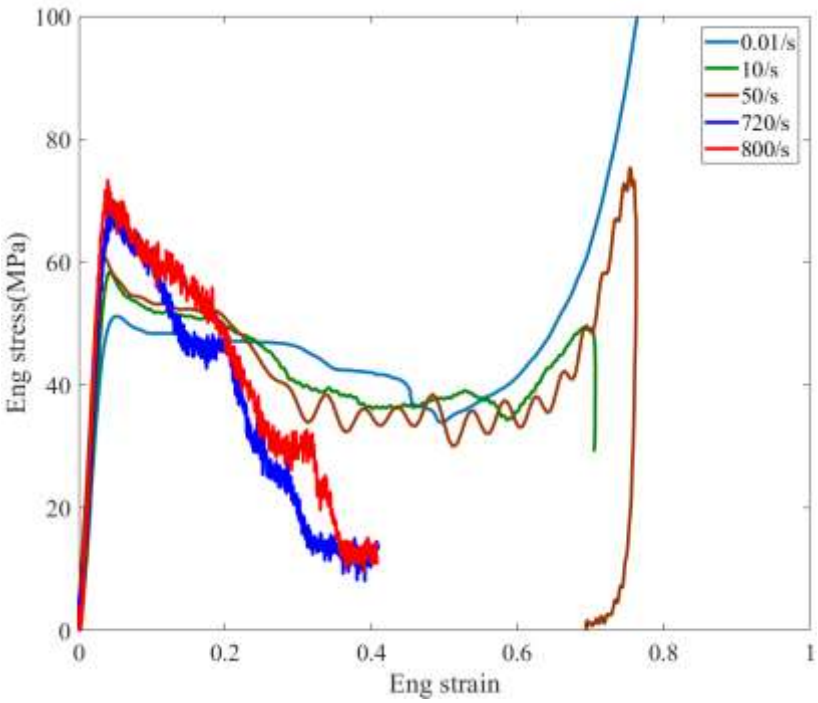

(a)Without confinement

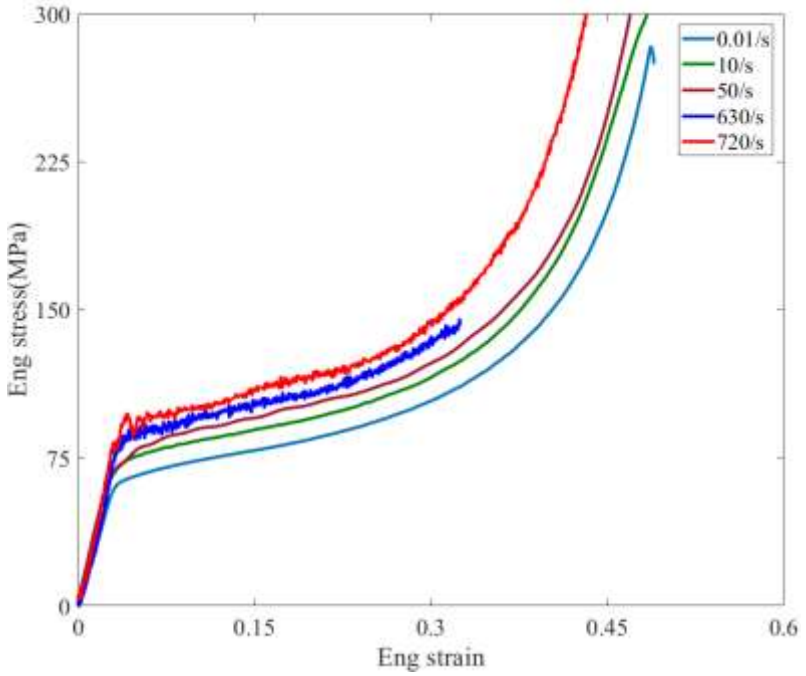

(b) With confinement

Fig.11 Engineering stress-strain relationship for unconfined and confined ESF specimens from low to high strain rates at room temperature

The typical engineering stress evolution at high strain rate of 600 /s and room temperature is shown Fig.12a, with the corresponding deformation process from the

high-speed DIC analysis in Fig.12b. An almost homogeneous deformation in elastic part can be seen at stage 2. After the peak stress at stage 3, a localization firstly occurs at the bottom side of the specimen marked by a white arrow at stage 4. This is followed by the propagation of the localization towards the upper side at stage 5. Thereafter, localization at the bottom side appears again adjacent to the first localization area at stage 6. With continuous deformation and decreasing stress, further localization can be observed with localized bands at stage 7. Following the localization paths, the specimen collapsed completely with several fragments indicated at stage 8. The deformation history clearly shows the elastic-brittle behavior of ESF at high strain rate associated with shear localization.

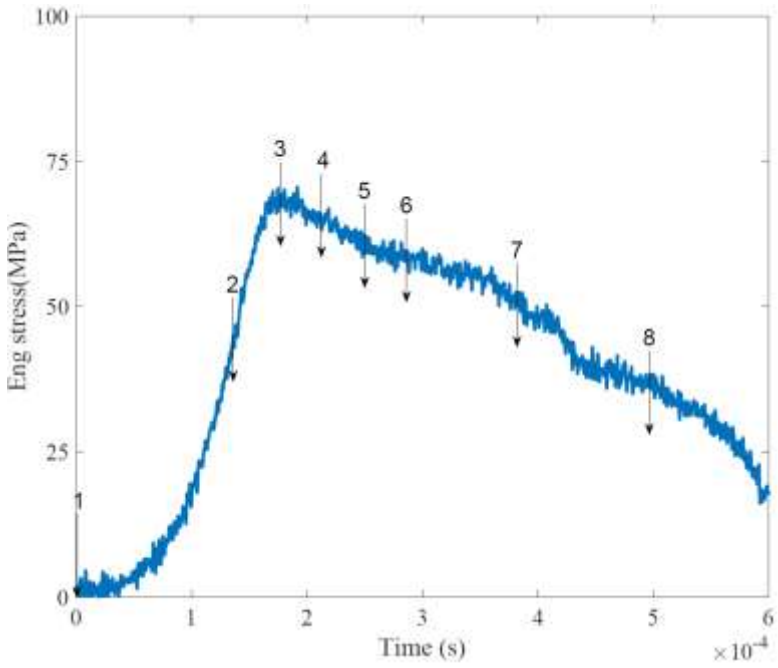

(a)Macro engineering stress history with different stages at room temperature

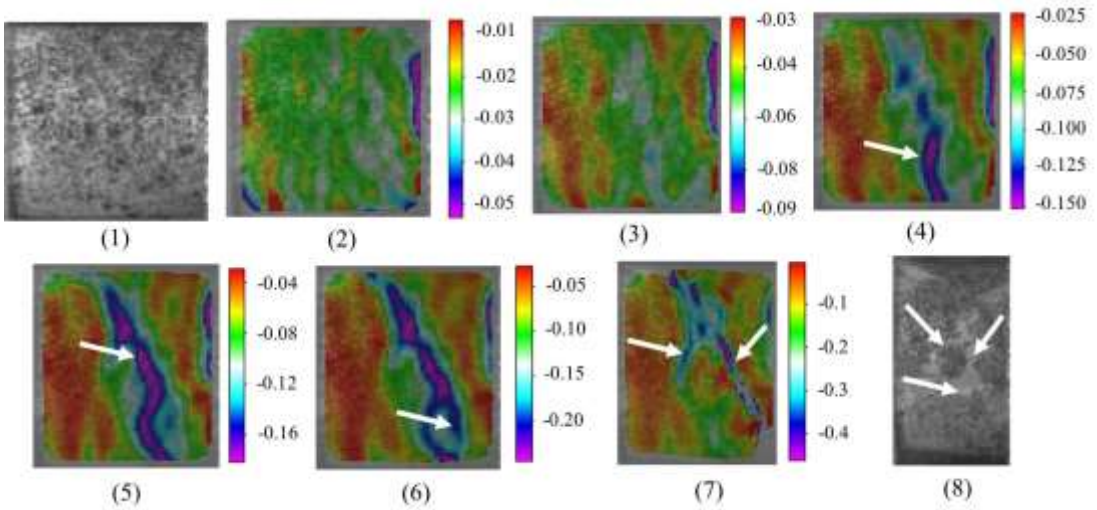

(b) Deformation process from DIC analysis with the axial engineering strain field

Fig.12 Typical engineering stress as a function of time, together with the corresponding strain filed from DIC analysis at high strain rate of 600 /s and room temperature

The macro engineering stress and the deformation process with DIC analysis at high strain rate of 800 /s and 150 ℃ are shown in Fig.13. Followed by the initial peak stress, the macro stress drops slightly from stage 3 to stage 5. Localization can be observed at stage 4 from the DIC analysis. Beyond the plateau stress at stage 5, the macro stress shows strain hardening while the DIC analysis within the dashed rectangle area presents a relatively uniform deformation at stage 6 and stage 7. The fracture (white arrow) finally occurs at the center of the specimen.

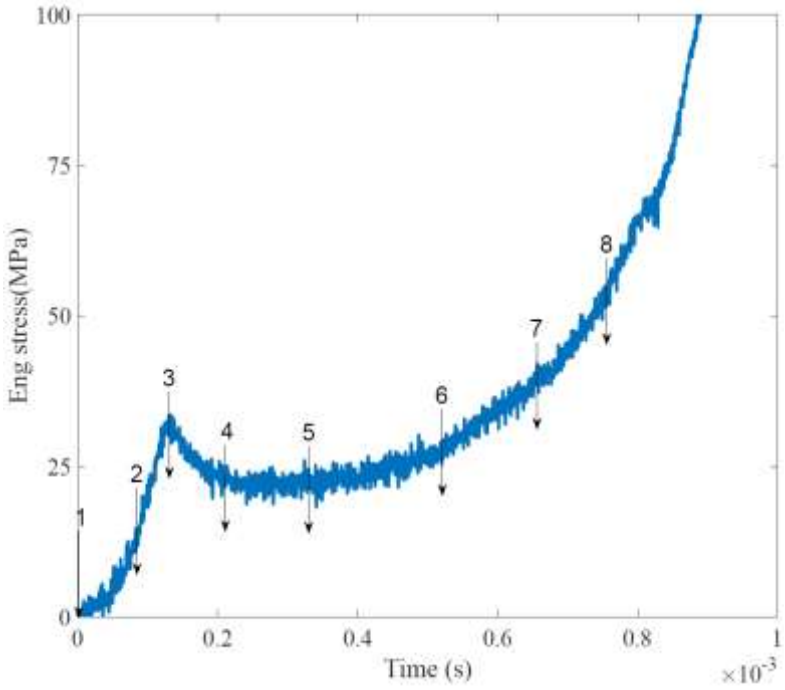

(a)Macro engineering stress history with different stages

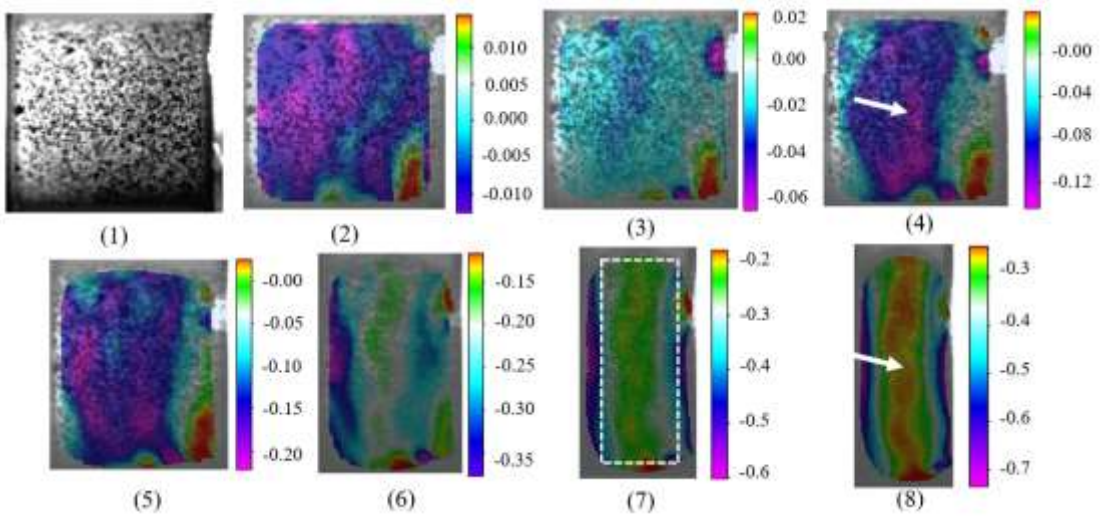

(b) Deformation process from DIC analysis with the axial engineering strain field

Fig.13 Typical engineering stress as a function of time, together with the corresponding axial engineering strain filed from DIC analysis at high strain rate of 800 /s and 150 ℃

Considering the influence of strain rate on the yield stress evolution, Fig.14 compares the yield stress of ESF with and without confinement as a function of logarithmic strain rate. The confined yield stress is slightly higher than the unconfined yield stress

across five orders of magnitude strain rate regions. In previous studies of syntactic foams [20, 21, 35, 36] , there is a lack of test data at medium rates (1-100 /s). By using the Instron machine, the present work is able to report data in strain rate gap between quasi-static and high strain rate regions, thereby, providing more information for a better understanding of the strain rate dependency of syntactic foam.

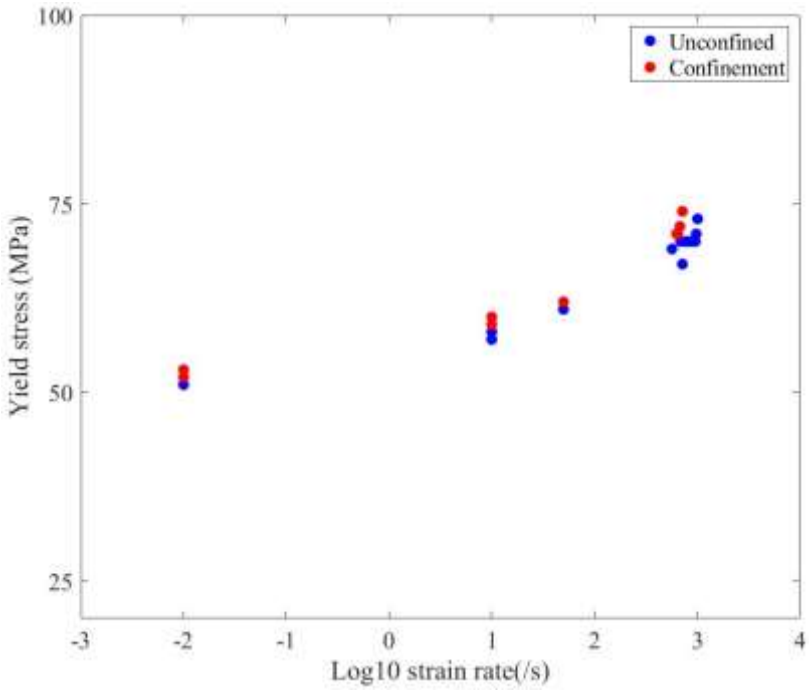

Fig. 14 Plot of yield stress vs. strain rate for unconfined and confined ESF specimens at room temperature

Considering the strain rate effect on energy absorption, Fig.15 shows the energy density of unconfined and confined ESF as a function of logarithmic strain rate. The first observation is that the energy density for confined ESF is consistently higher than that without confinement. The confined energy density increases from 33 J/m^3 at quasi-static to 38 J/m^3 at high strain rates, while the unconfined energy density decreases significantly from 25 J/m^3 at quasi-static to 14 J/m^3 at high strain rates.

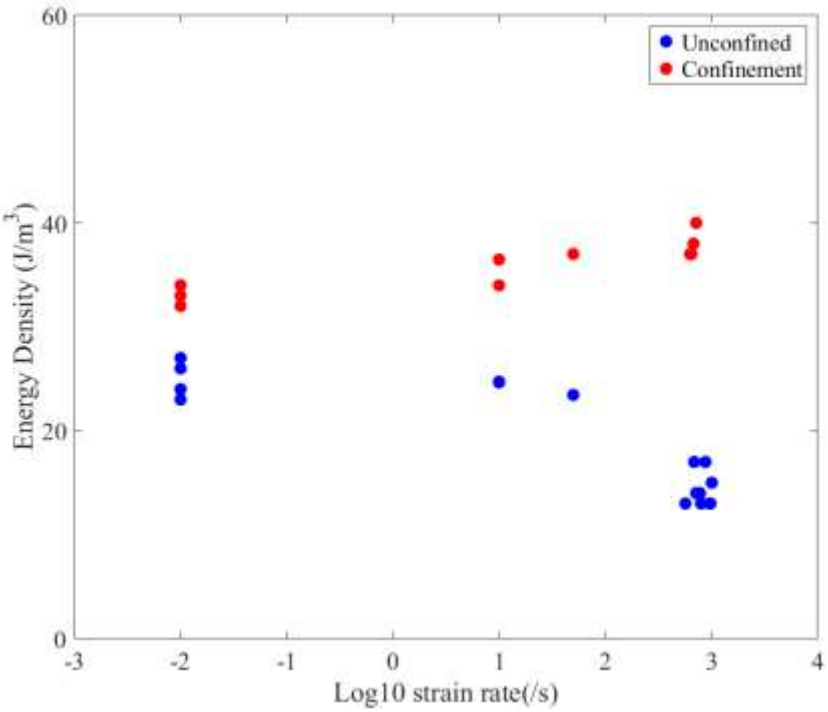

Fig. 15 Plot of energy absorption vs. strain rate for unconfined and confined ESF specimens at room temperature

3.3 High Strain Rate Results at Elevated Temperatures

Fig.16 shows the temperature dependent engineering stress-strain relationship at high strain rates without confinement and with confinement. The unconfined stress-strain relationships at room temperature and 65 ℃ show elastic-brittle behavior with significant load drop after the peak stress. Compared to the response at room temperature, the stress-strain relationship at 65 ℃ shows a slower decreasing stress, but still loses the load bearing capacity. Starting from the temperature 100 ℃, the stress-strain relationship presents increasing strain hardening and the densification stage can be seen beyond a strain of about 0.65. With an increase in temperature, the peak stress decrease. This is followed by strain softening of the material. The stress-strain relationship at 125 ℃ and 150 ℃ show gradual strain hardening from a strain of 0.25.

The confined yield stress decreases with the increase of the temperature at high strain rates. Specifically, the yield stress 71MPa at room temperature gradually decreases to

37 MPa at 150 ℃. No strain softening can be seen in the confined behavior, which is different from that without confinement. The engineering stress-strain relationship at room temperature shows apparent strain hardening in the plastic region. With the increase of temperature, the plastic region seems to present a slightly decreasing strain hardening. Consequently, the role of temperature in decreasing the yield stress is the same for unconfined and confined stress-strain relationship, while its influence on strain hardening appears to be slightly different.

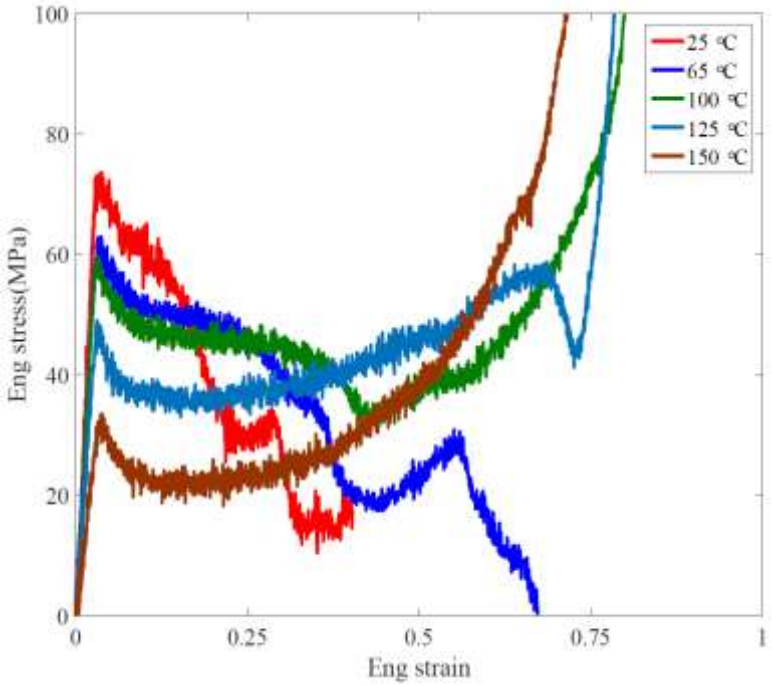

(a)Unconfined

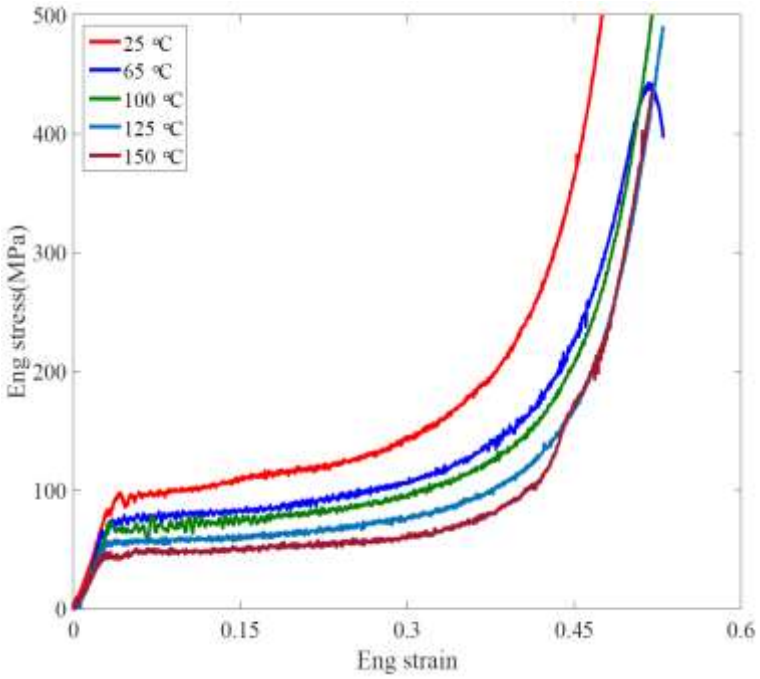

(b) Confined

Fig. 16 Engineering stress-strain relationship of ESF without confinement and with confinement at high strain rates under different temperature conditions

Fig.17 compares the energy density of unconfined and confined ESF as a function of temperature at high strain rates. The energy density of ESF with lateral confinement is generally higher than that of unconfined ESF from room temperature to elevated temperatures. The energy density for confined ESF gradually decreases from 38 J/m^3 at room temperature to 20 J/m^3 at elevated temperature of 150 ℃. For ESF without confinement, the energy density firstly increases from 14 J/m^3 at room temperature to 25 J/m^3 at elevated temperature of 100 ℃, then decreases to 13 J/m^3 at elevated temperature of 150 ℃.

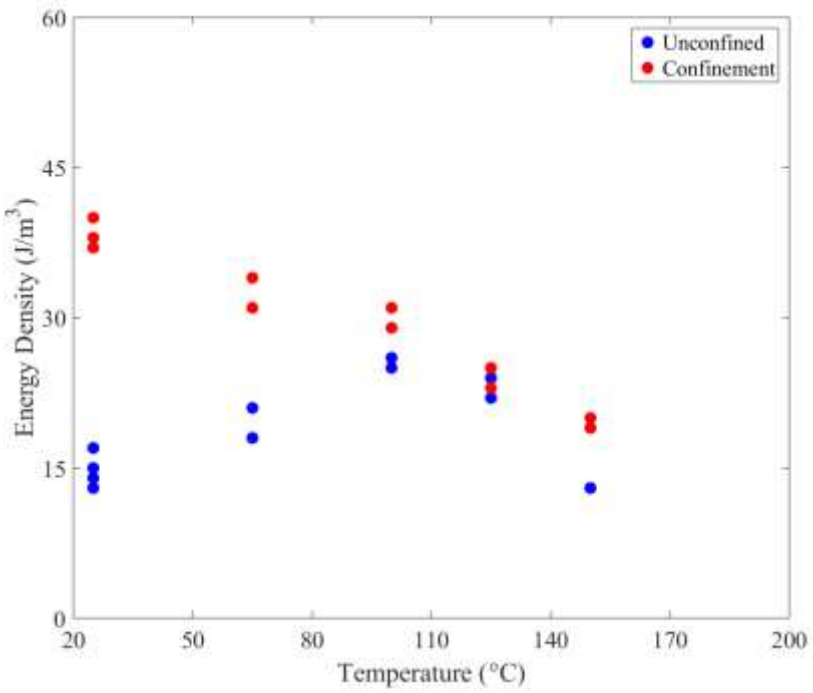

Fig. 17 Plot of energy absorption vs. temperature for unconfined and confined ESF specimens at high strain rates.

3.4 Microstructural Characterization

The fracture morphology of ESF specimens was characterized by using a Carl Zeiss Evo LS 15 VP-Scanning Electron Microscope at low (x370) and high (x1000) magnification levels. Fig.18a shows fracture surface of a large strain compressed specimen fractured at quasi-static loading and room temperature with fully densification. The region which consists of collapsed microballons and matrix is marked by a red arrow in Fig.18a, with a higher magnification in Fig.18b. Fig.18 (c-d) present fracture surface at two magnification levels for the specimen failed at medium rate of 10 /s and room temperature, in which the microstructure shows deformed and fractured microballons. Similar observation can be seen for the specimen failed at high strain rate of 800 /s and room temperature in Fig.18 (e-f). This corresponds to the localization failure mode and the following fragmentation of the specimen (Fig.12), resulting in localized failed regions and partly deformed regions [37].

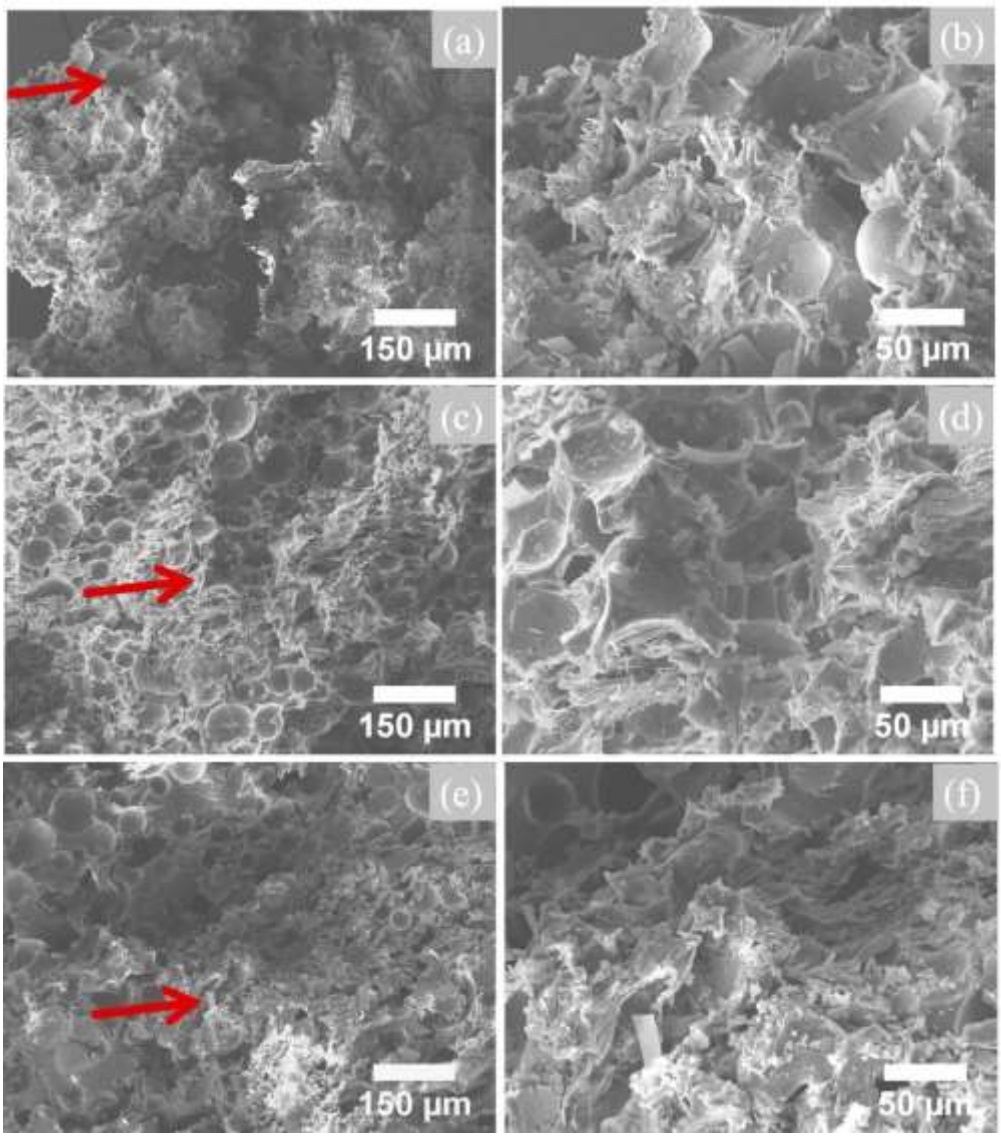

Fig.18 Comparison of fractographic images at two magnification levels (x380 and x1000) for unconfined specimens tested at room temperature under (a-b) quasi-static, (c-d) medium rate, (e-f) high strain rate loading conditions. The marked area is shown at a higher magnification (x1000).

In addition to the above microstructural characterization for the fractured specimens at room temperature, Fig.19 compares the fracture surfaces for the specimens dynamically failed at elevated temperatures of 65 ℃, 100 ℃, 125 ℃ and 150 ℃ at two magnification levels respectively. The microstructure for the fractured specimen tested at 65 ℃ presents localized failed regions and severely deformed regions in

Fig.19a, and the marked area with collapsed microballons is magnified in Fig.19b. This micrograph corresponds to the same dynamic strain localization failure mode as that in the specimen dynamically failed at room temperature in Fig.18e. However, with the increase of temperature above 100 ℃, the elastic-brittle response of ESF gradually transforms to flexible (rubber type) behavior. The fracture morphology of specimens dynamically tested at elevated temperatures of 100 ℃, 125 ℃ and 150 ℃ is featured by complete collapsed microballons and matrix. The marked areas in Fig.19(c, e, g) are magnified in Fig.19 (d, f, h). It is found that these microstructures are generally similar to the complete fracture features with a large amount of debris in Refs. [11, 37-39].

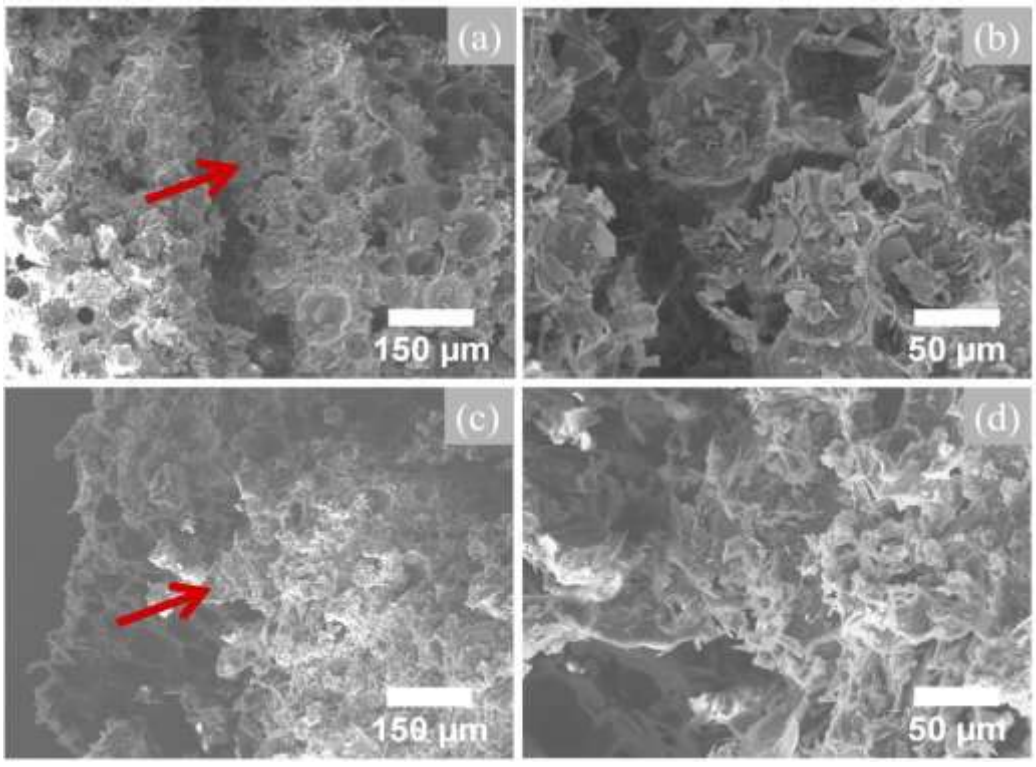

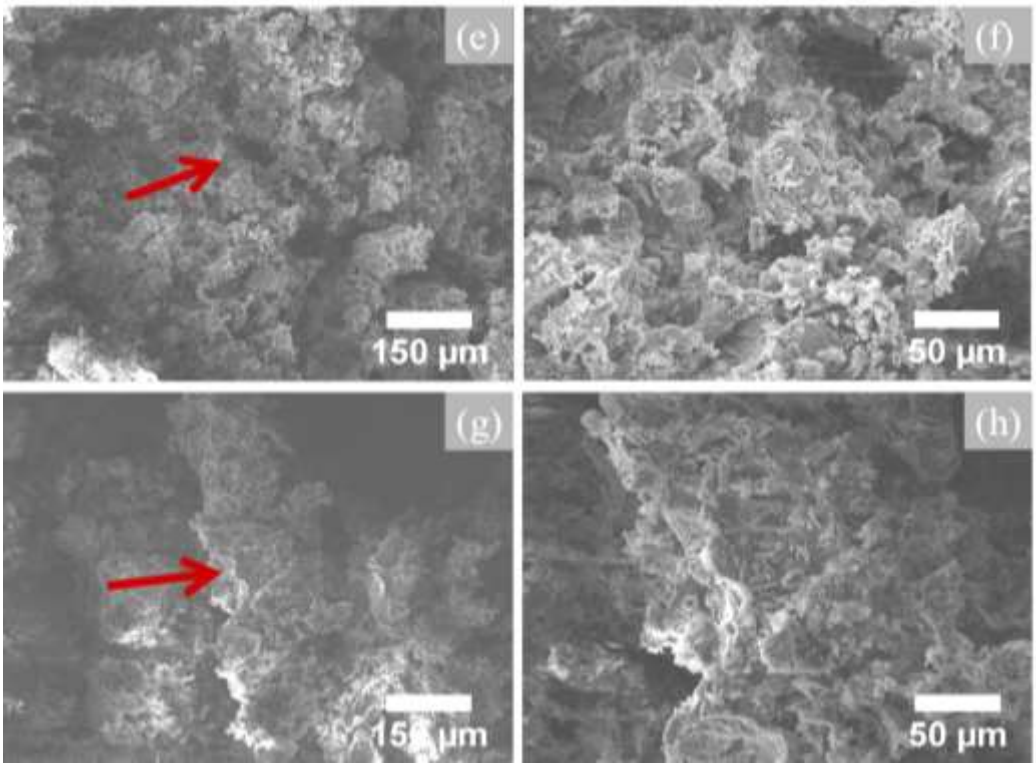

Fig.19 Comparison of fracture morphology at two magnification levels for unconfined specimens dynamically tested at elevated temperatures (a-b) 65 ℃, (c-d) 100 ℃, (e-f) 125 ℃, (g-h) 150 ℃. The marked area is shown at a higher magnification.

The confined specimens were constrained inside the rigid tube without failure. Fig.20 typically compares the microstructures of confined specimens dynamically loaded at room temperature and elevated temperature of 150 ℃. After large strain deformation, the microstructure for the confined specimen at room temperature is presented in Fig.20a, with a higher magnification image for the crushed and compacted microballons shown in Fig.20b. However, more partially deformed microballons without complete fracture can be clearly seen in the confined specimen tested at elevated temperature of 150 ℃ in Fig.20c and Fig.20d at two magnification levels.

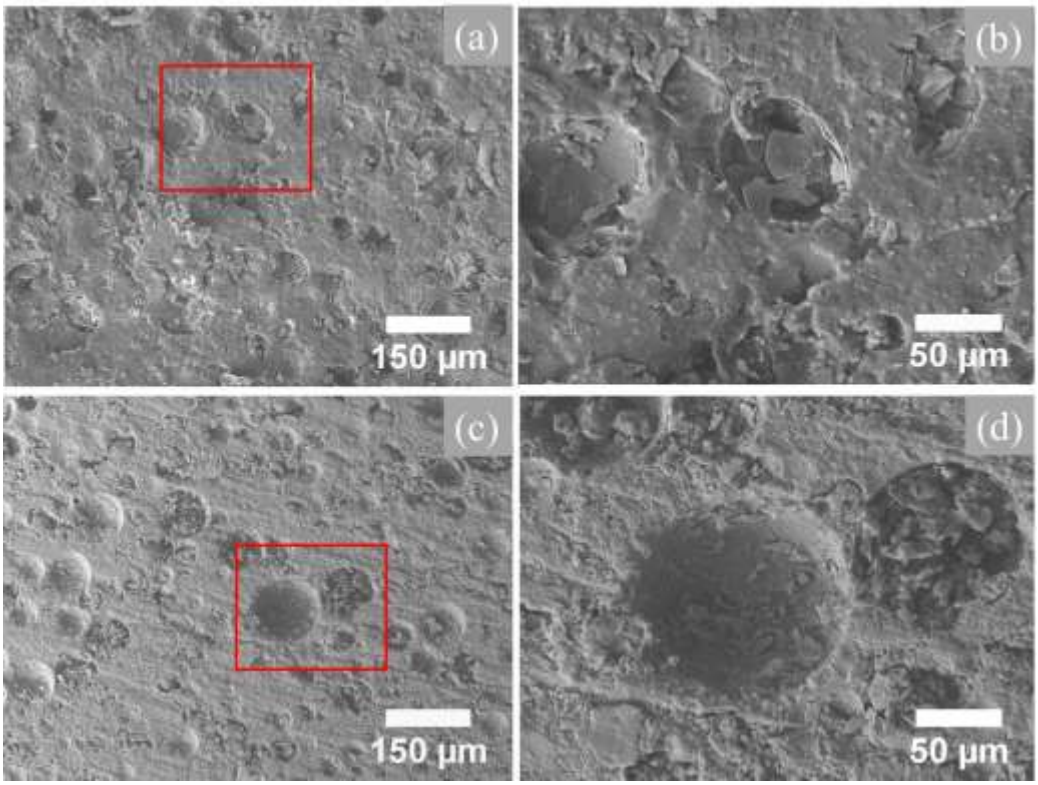

Fig.20 Fracture morphology at two magnification levels for confined specimens tested at high strain rate at (a-b) room temperature, and (c-d) elevated temperature of 150 ℃.

4. Analysis of Constitutive Response

The constitutive response of the ESF is analyzed to provide guidance for the further numerical simulation of structural impact applications. The strain rate and temperature sensitivities, and the strain hardening/softening evolution of the ESF will be analyzed in this section.

4.1 Strain rate sensitivity

To quantitatively describe the strain rate dependency, a model to determine the strain sensitivity of ESF fam is defined as follows：

$$\sigma=\sigma_0[1+\varphi\left(\frac{\dot{\varepsilon}}{\dot{\varepsilon}_0}\right)^{\omega}] \tag{1}$$

where σ_0 is the yield stress at a reference strain rate $\dot{\varepsilon}_0$=0.01 /s, $\dot{\varepsilon}$ is the strain rate, φ and ω are the parameters describing the strain rate sensitivity. The fitted models for are $\sigma=51[1+0.0278\left(\frac{\dot{\varepsilon}}{\dot{\varepsilon}_0}\right)^{0.2297}]$ and $\sigma=52[1+0.0217\left(\frac{\dot{\varepsilon}}{\dot{\varepsilon}_0}\right)^{0.2589}]$ for unconfined and confined ESF respectively. The yield stress evolves nonlinearly as a function of logarithmic strain rate, as can be seen in Fig.21.

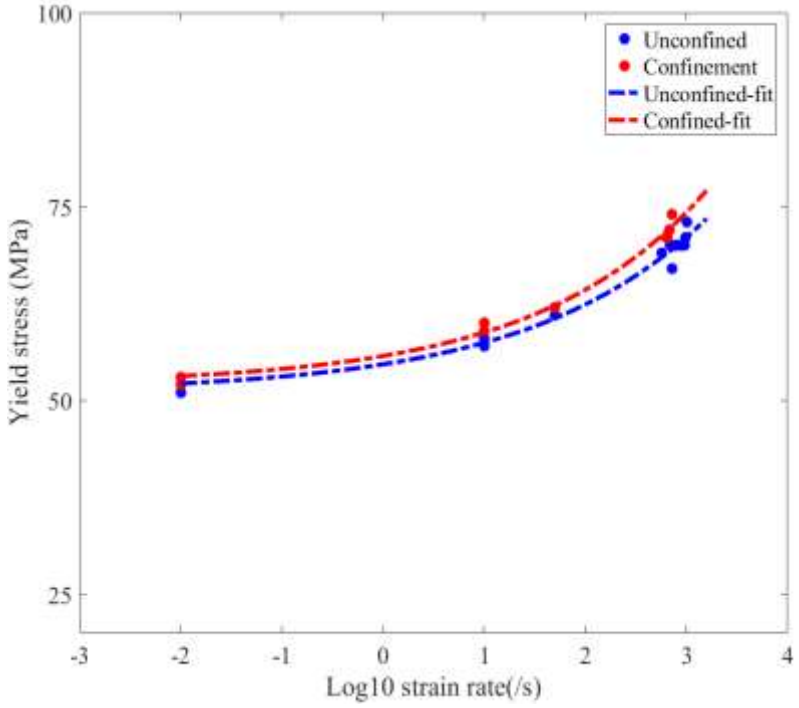

Fig.21 Strain rate dependent yield stress for ESF foam at room temperature.

4.2 Temperature sensitivity

Considering the temperature sensitivity, Fig.22 presents the yield stress of ESF foam at high strain rates for different temperature conditions. Here, a thermal softening model is employed to describe the temperature sensitivity of ESF, which is given by

$$\sigma=\sigma^0\left[1-n\left(T-T_r\right)^m\right] \quad (2)$$

where σ^0 is the yield stress at high strain rates of about 600-800 /s, T_r is the reference temperature 25 ℃, n and m are the parameters describing the temperature sensitivity. The trend of decreasing yield stress with the increase of temperature is similar for unconfined and confined ESF, consequently all experimental data of yield stress are used to calibrate the formulation. One can find that the thermal softening model $\sigma=70\left[1-0.0000703\left(T-T_r\right)^{1.8265}\right]$ is able to describe the nonlinear decreasing yield stress as a function of the temperature.

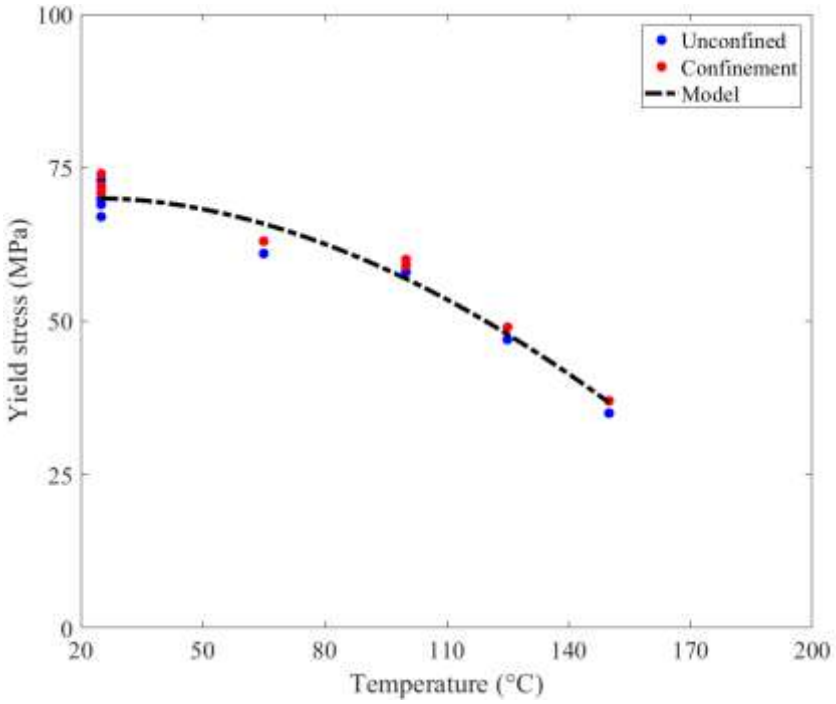

Fig.22 Temperature dependent yield stress for ESF foam at different temperatures and high strain rates of 600-800 /s.

4.3 Analysis of strain hardening evolution

A simple formulation with limited constants would be desirable for the description of the constitutive response of the ESF. Here, a phenomenological model with six constants proposed by Liu [21, 40] is employed for the description of the constitutive response of the present ESF as follows:

$$\sigma = \mathrm{A}\frac{e^{\alpha\varepsilon}-1}{1+e^{\beta\varepsilon}} + Ke^{\mathrm{C}}(e^{\gamma\varepsilon}-1) \quad (3)$$

The parameter A has units of stress and the parameter K is for the consistency of stress unit. The parameters α and β in the first term describe the nonlinear behavior of the foam. The case $\alpha=\beta$ corresponds to ideal plastic response, while $\alpha<\beta$ and $\alpha>\beta$ represent the strain softening behavior and the strain hardening behavior respectively. The two parameters C and γ in the second term describe the densification stage with rapidly increasing stress.

At quasi-static and medium rates in Fig.23a, the full terms in equation (3) are used for the constitutive description of the unconfined ESF. At high strain rates, the first term in equation (3) with three constants A, α and β is sufficient to analyze the response of unconfined ESF. The calibrated constants are shown in Table 2. The parameters $\alpha<\beta$ are consistent for unconfined ESF over various strain rates, indicating the strain softening deformation.

Fig.23b shows the nonlinear constitutive description for confined ESF, and the calibrated constants are given in Table 2. The parameters $\alpha>\beta$ indicate the strain hardening behavior in confined ESF. This is different from the response in unconfined ESF. Densification stages can be seen for all confined specimens, and the full terms in equation (3) are used to describe the large deformation behavior.

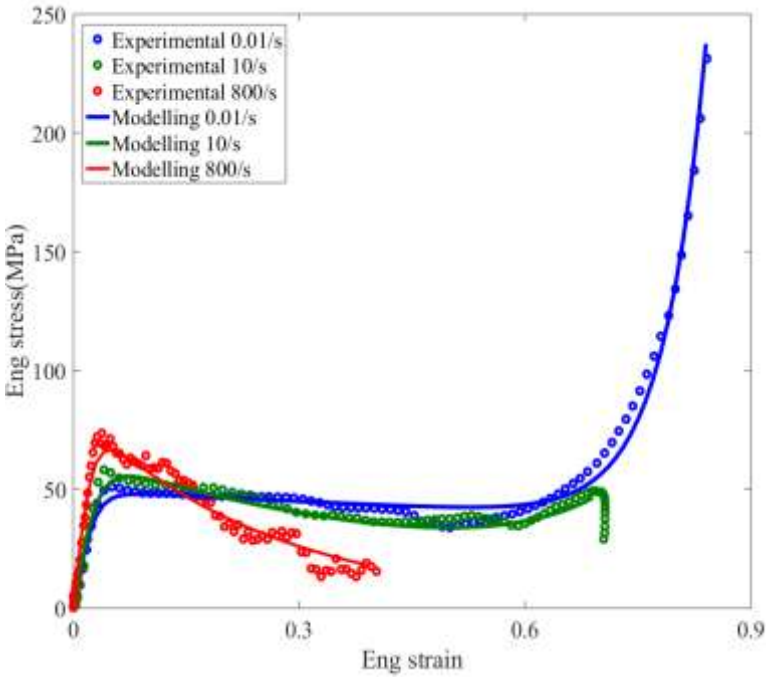

(a)

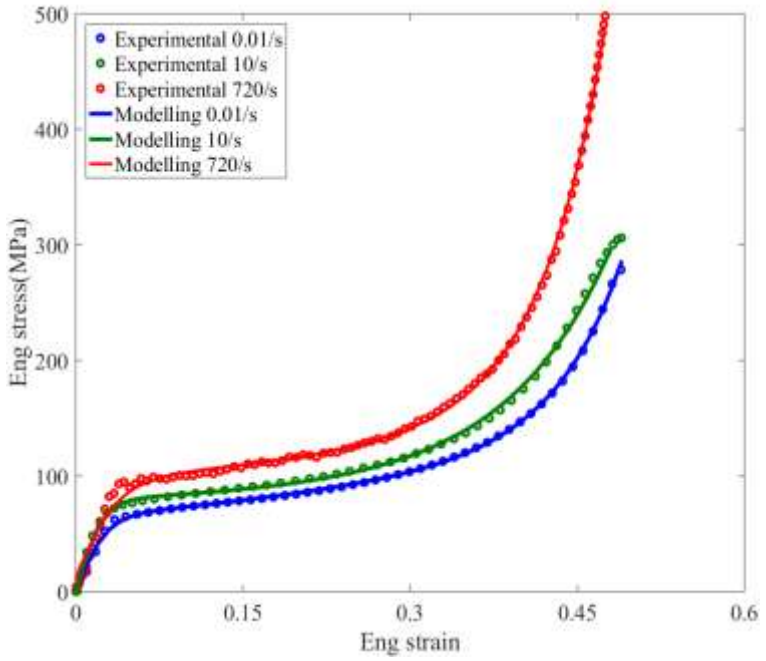

(b)

Fig.23 Comparison of the stress-strain relationship between the model description and the experimental data for the ESF without confinement (a) and with confinement (b) at room temperature.

Unconfined						
Condition	A(MPa)	α		β	C	γ
0.01 /s	49.62	70.18	<	70.51	-9.53	17.65
10 /s	64.31	57.87	<	59.53	-2.078	7.741
800 /s	85	72.73	<	76.68	-	-
Confined						
Condition	A(MPa)	α		β	C	γ
0.01 /s	63.79	74.85	>	73.46	-3.004	16.49
10 /s	78.85	85.95	>	85.52	0.1262	10.78
720 /s	94.83	50.34	>	49.47	-2.312	16.99

Table 2. Constants in the nonlinear model for unconfined and confined ESF at room temperature. Note the differences in the strain softening in unconfined ESF and the strain hardening in confined ESF, as indicated by the competition between the parameters α and β.

The effect of temperature on the stress-strain relationship at high strain rates is presented in Fig.24, together with the model descriptions at room temperature 25 ℃, 100 ℃ and 150 ℃. The corresponding constants are listed in Table 3. At room temperature, the parameter α is smaller than the parameter β for unconfined foam. At an elevated temperature of 100 ℃, the parameter β 66.58 evolves closer to the parameter α 65, indicating the gradually decreasing strain softening in unconfined foam. At a higher temperature of 150 ℃, one can find that $\alpha > \beta$ with the values 102.4 and 102.2 respectively. The macro stress-strain relationship shows strain hardening in most of the plastic deformation stage.

Difference occurs in confined foam at high strain rates from room temperature to elevated temperatures. Table 3 shows that the parameter α is consistently higher than the parameter β, indicating the strain hardening deformation. The difference between two parameters α and β is gradually *smaller* with the increase of temperatures. The

parameter α 82.39 is very close to the parameter β 82.02 at a high temperature of 150 ℃. The elevated temperatures gradually decrease the strain hardening for the confined foam at high strain rates.

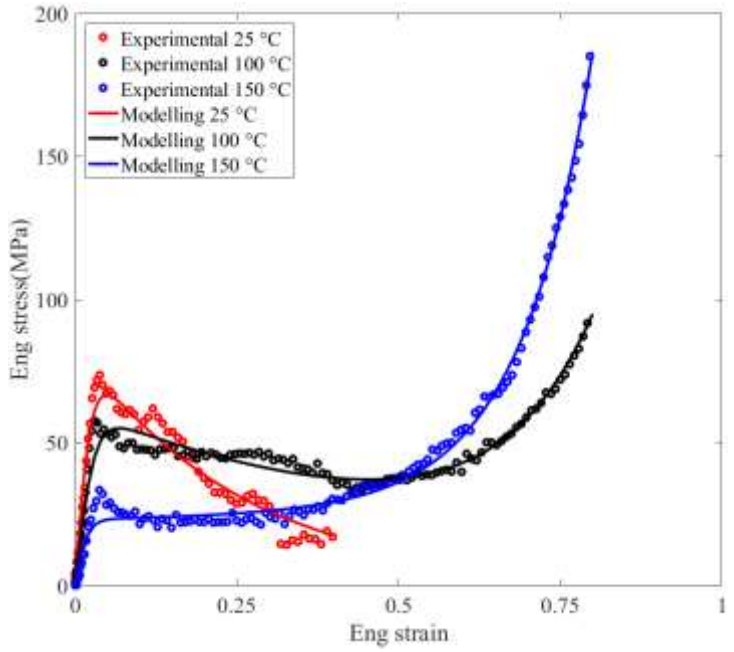

(a)

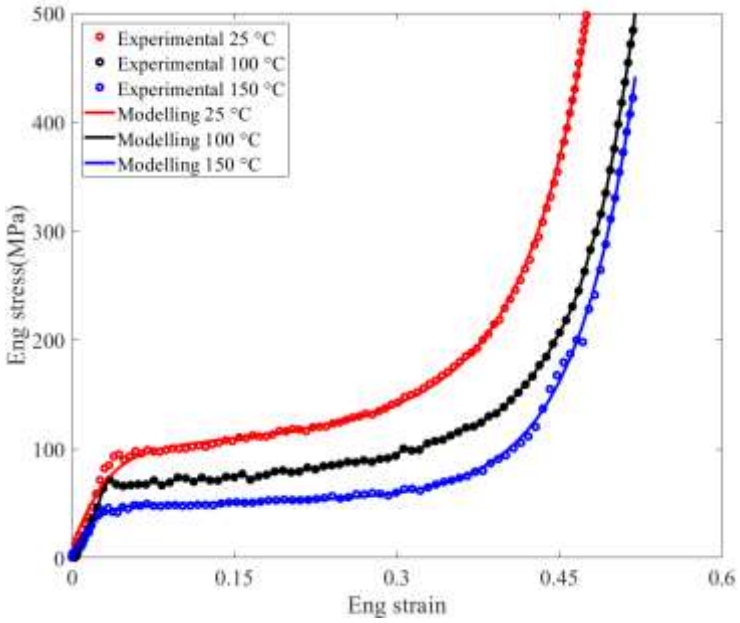

(b)

Fig.24 Comparison of the high strain rate stress-strain relationship between the model description and the experimental data for the ESF without confinement (a) and with confinement (b) at different temperatures

Unconfined						
Condition	A(MPa)	α		β	C	γ
25 ℃	85	72.73	<	76.68	-	-
100 ℃	62.46	65	<	66.58	-1.254	7.006
150 ℃	23.03	102.4	>	102.2	-2.083	8.943
Confined						
Condition	A(MPa)	α		β	C	γ
25 ℃	94.83	50.34	>	49.47	-2.312	16.99
100 ℃	64.43	71.1	>	70.03	-3.726	18.6
150 ℃	47.55	82.39	>	82.02	-3.619	18.4

Table 3. Constants in the nonlinear model for unconfined and confined ESF at different temperatures and high strain rates

Recently, Arezoo et al. [15] investigated the time–temperature superposition of the foam in which the temperature sensitivity was corrected to strain rate dependent elastic-plastic response. Here, it would be worthwhile to investigate the similar behavior of the present ESF. Fig.25 shows the stress-strain relationship at medium rate of 10-50 /s tested at room temperature, and the stress-strain relationship at high strain rate of 820 /s tested at 100 ℃. The model description is also added for the quantitative comparison. Visually, these stress-strain relationships are very similar, in terms of yield stress, strain softening and densification. The six parameters in equation (3) are also quantitatively similar, with the parameters A equal to 64.31 and 62.46 respectively. The parameter β is slightly higher than the parameter α, indicating the softening plastic response at medium rate of 10-50 /s and room temperature, and at high strain rate of 820 /s and 100 ℃.

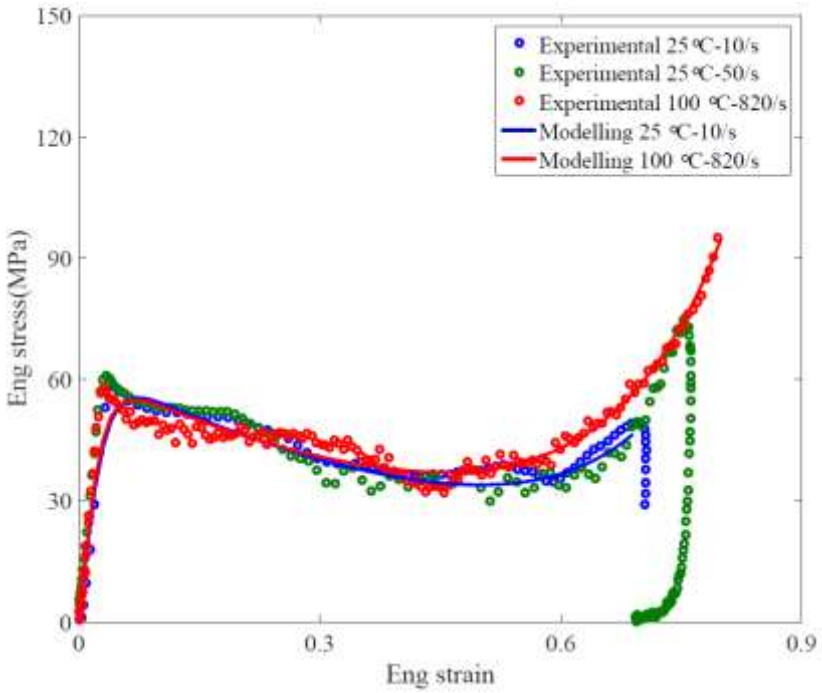

Fig.25 Typical engineering stress-strain relationship at medium rate and room temperature, and high strain rate and high temperature 100 ℃.

5. Discussion

This paper reports the large deformation and failure behavior of an ESF from low to high strain rates and different temperatures. This material is being increasingly used in the design of jet engine fan containment system to improve the structural impact resistance, e.g. against bird strike events and blade off events. The dynamic strain localization in unconfined ESF is monitored by using a bespoke designed Hopkinson bar technique synchronized with a high-speed camera and equipped with an environmental chamber. The stress concentration at specimen ends would increase the measured stress of the specimen [41] and influence the understanding of the rate dependency and the actual failure mode of the foam materials. In the present work, uniform deformation in the specimen can be seen from DIC analysis. The shear strain localization initiates at the center of specimen, which is the dominant failure mode of the unconfined foam at high strain rates, as reported by Gupta et al. [42], Rittel [13], and recently by Li et al. [14] and Pellegrino et al. [18]. The microstructure for the dynamically failed specimen at room temperature presents localized regions, severely

deformed and fractured microballons, which correspond to the elastic-brittle behavior and strain localization failure mode. With the increase of temperature above 100 ℃, the elastic-brittle behavior is suppressed, and the fracture morphology in large strain compressive specimens is featured by complete collapsed microballons and matrix with a large amount of debris (Fig.19). At elevated temperatures and high strain rates, the brittle behavior of ESF transformed to flexible (rubber type) response. Similar changes in the behavior were reported by Song et al. [38] in the syntactic foam specimens tested at high strain rates and high temperatures, due to the fewer connecting microspheresites and a smaller number of microcracks.

Different from the unconfined ESF foam which shows strain softening behavior after the peak stress at high strain rate tests performed at room temperature, the confined ESF foam shows larger deformation without macro failure up to the strain of 0.5. With the introduction of confinement to restrict the radial strain, the ESF deforms plastically up to densification stage. The lateral confinement maintains the damaged material to move away, consequently, the flow stress in confined ESF increases continuously during the strain hardening deformation, which agrees with the findings in Ref. [20]. Analysis of densification mechanics shows that the energy absorption for confined ESF is consistently higher than that without confinement. Compared to the unconfined ESF with brittle behavior at high strain rates, the lateral confinement increases the energy absorption by a factor of 2.7, by compacting the deformed matrix and damaged microballons (Fig.20a-b) and increasing the bulk density. This eventually strengthens the material and result in higher energy absorption. It would be desirable for the application of confined ESF in aerospace engineering to improve the load bearing and energy absorption capabilities during impact events.

The nonlinear increasing strain rate and decreasing temperature sensitivities are analyzed for unconfined and confined foams. A nonlinear model in equation (3) [21, 40] with limited constants is used to describe the elastic-brittle without confinement and elastic-plastic behavior under confinement across various strain rates and temperatures. The evolution of strain hardening and strain softening are compared. It is found that the strain hardening capacity of unconfined ESF increases with

increasing temperature, while the strain hardening capacity of confined ESF slightly decreases with increasing temperature particularly at 125 ℃ and 150 ℃. The energy density also decreases with the increase of temperature particularly at elevated temperatures of 125 ℃ and 150 ℃. Noted that these temperatures are close to or higher than the glass transition temperature of the investigated ESF. The epoxy matrix material is inherently temperature dependent, consequently, the elevated temperatures would affect the strain hardening of confined ESF at high strain rates, as indicated by Arezoo et al. [15]. After almost full recovery, the microstructure in the confined specimen at 150 ℃ shows more microballons without complete fracture (Fig.20c-d) than that at room temperature (Fig.20a-b), indicating the density of the confined foam at high temperature is maintained at a lower level compared to that at room temperature. This also offers additional insight into the slightly lower strain hardening in the confined specimen at elevated temperatures.

Further work will aim at investigating the potential adiabatic temperature rise at high strain rates for a better understanding of the dynamic response of the ESF material. Likewise, the comparison of the mechanical behavior of the ESF under different loading modes will be studied. Given the potential ice accumulation on the engine components which would impact the fan containment system, the response of ESF under confinement and low temperature conditions will be investigated in the future.

6. Conclusion

This paper presents the constitutive response and failure of an unconfined and confined ESF at quasi-static, medium rate and high strain rates at gradually increasing temperatures from 25 ℃ to 150 ℃. The stress-strain relationships of ESF without and with confinement display similar nonlinear strain rate and temperature dependencies. DIC analysis shows uniform deformation within the specimen, and the shear strain localization initiates at the center of unconfined ESF at high strain rates and room temperature. With the introduction of rigid confinement, the stress-strain relationship shows elastic-plastic response and strain rate independent strain hardening. The lateral confinement also slightly increases yield stress but apparently increases the energy

absorption of ESF. The elevated temperatures and lateral confinement suppress the elastic-brittle behavior of unconfined ESF at high strain rates. The temperature plays a role in increasing the strain hardening in unconfined ESF at high strain rates, while it slightly decreases the strain hardening for the confined ESF. A phenomenological model is able to describe the elastic-brittle behavior and elastic-plastic behavior for the unconfined and confined ESF foam at various strain rates and temperatures, and provides quantitative information on the strain hardening/softening evolution.

Acknowledgements:

The assistance from Mr. P. Tantrum, Mr. S. Carter, Dr. K. Dragnevski, Mr. N. Hawkins and Mrs. K. Bamford is greatly appreciated. Likewise, Mr. A. Lui and Dr. K. Liu are acknowledged for the X-Ray CT scan analysis.

Declaration of interests

There is no conflict of interest. The authors declare that they have no known competing financial interests or personal relationships or that could have appeared to influence the work reported in this paper

References:

[1] F.A. Shutov, Syntactic polymer foams, Chromatography/foams/copolymers, (1986) 63-123.

[2] L.J. Gibson, Cellular solids, Mrs Bulletin, 28 (2003) 270-274.

[3] N. Gupta, S.E. Zeltmann, V.C. Shunmugasamy, D. Pinisetty, Applications of polymer matrix syntactic foams, Jom, 66 (2014) 245-254.

[4] L.J. Gibson, M.F. Ashby, Cellular Solids: Structure and Properties, 2 ed., Cambridge University Press, Cambridge, 1997.

[5] N. Mills, C. Fitzgerald, A. Gilchrist, R. Verdejo, Polymer foams for personal protection: cushions, shoes and helmets, Composites science and technology, 63 (2003) 2389-2400.

[6] M.F. Ashby, R.M. Medalist, The mechanical properties of cellular solids,

Metallurgical Transactions A, 14 (1983) 1755-1769.

[7] P. Bunn, J. Mottram, Manufacture and compression properties of syntactic foams, Composites, 24 (1993) 565-571.

[8] E.M. Wouterson, F.Y. Boey, X. Hu, S.-C. Wong, Specific properties and fracture toughness of syntactic foam: Effect of foam microstructures, Composites science and technology, 65 (2005) 1840-1850.

[9] N. Gupta, W. Ricci, Comparison of compressive properties of layered syntactic foams having gradient in microballoon volume fraction and wall thickness, Materials Science and Engineering: A, 427 (2006) 331-342.

[10] J. Adrien, E. Maire, N. Gimenez, V. Sauvant-Moynot, Experimental study of the compression behaviour of syntactic foams by in situ X-ray tomography, Acta Materialia, 55 (2007) 1667-1679.

[11] B. Song, W. Chen, D.J. Frew, Dynamic Compressive Response and Failure Behavior of an Epoxy Syntactic Foam, Journal of Composite Materials, 38 (2004) 915-936.

[12] G. Subhash, Q. Liu, X.-L. Gao, Quasistatic and high strain rate uniaxial compressive response of polymeric structural foams, Int. J. Impact Eng, 32 (2006) 1113-1126.

[13] D. Rittel, Adiabatic shear failure of a syntactic polymeric foam, Mater Lett, 59 (2005) 1845-1848.

[14] P. Li, N. Petrinic, C.R. Siviour, R. Froud, J.M. Reed, Strain rate dependent compressive properties of glass microballoon epoxy syntactic foams, Materials Science and Engineering: A, 515 (2009) 19-25.

[15] S. Arezoo, V.L. Tagarielli, C.R. Siviour, N. Petrinic, Compressive deformation of Rohacell foams: Effects of strain rate and temperature, Int. J. Impact Eng, 51 (2013) 50-57.

[16] S. Arezoo, V. Tagarielli, N. Petrinic, J. Reed, The mechanical response of Rohacell foams at different length scales, Journal of materials science, 46 (2011) 6863-6870.

[17] T. Chu, W. Ranson, M.A. Sutton, Applications of digital-image-correlation

techniques to experimental mechanics, Exp Mech, 25 (1985) 232-244.

[18] A. Pellegrino, V.L. Tagarielli, R. Gerlach, N. Petrinic, The mechanical response of a syntactic polyurethane foam at low and high rates of strain, Int. J. Impact Eng, 75 (2015) 214-221.

[19] J. Liu, D. Saletti, S. Pattofatto, H. Zhao, Impact testing of polymeric foam using Hopkinson bars and digital image analysis, Polymer Testing, 36 (2014) 101-109.

[20] B. Song, W. Chen, T. Yanagita, D.J. Frew, Confinement effects on the dynamic compressive properties of an epoxy syntactic foam, Composite Structures, 67 (2005) 279-287.

[21] G. Subhash, Q. Liu, Quasistatic and dynamic crushability of polymeric foams in rigid confinement, Int. J. Impact Eng, 36 (2009) 1303-1311.

[22] R.M. Kully, Dynamic constitutive equation for a syntactic foam under multi-axial stress state, in, North Carolina Agricultural and Technical State University, 2014.

[23] D.L. Sutliff, M.G. Jones, Low-speed fan noise attenuation from a foam-metal liner, Journal of aircraft, 46 (2009) 1381-1394.

[24] D.L. Sutliff, M.G. Jones, T.C. Hartley, High-speed turbofan noise reduction using foam-metal liner over-the-rotor, Journal of Aircraft, 50 (2013) 1491-1503.

[25] B. Horton, J. Bayandor, Numerical investigation of fan-blade out using meso-scale composite modeling, in: 30th Congress of the International Council of the Aeronautical Sciences, ICAS, 2016, pp. 1-8.

[26] G. Quino, Y. Chen, K.R. Ramakrishnan, F. Mart ńez-Hergueta, G. Zumpano, A. Pellegrino, N. Petrinic, Speckle patterns for DIC in challenging scenarios: rapid application and impact endurance, Measurement Science and Technology, 32 (2020) 015203.

[27] L. Zhang, D. Rittel, S. Osovski, Thermo-mechanical characterization and dynamic failure of near α and near β titanium alloys, Mat Sci Eng a-Struct, 729 (2018) 94-101.

[28] L. Zhang, A. Pellegrino, D. Townsend, N. Petrinic, Thermomechanical Constitutive Behaviour of a Near α Titanium Alloy over a Wide Range of Strain Rates: Experiments and Modelling, International Journal of Mechanical Sciences, 189 (2020)

105970.

[29] R. Gerlach, C. Kettenbeil, N. Petrinic, A new split Hopkinson tensile bar design, Int. J. Impact Eng, 50 (2012) 63-67.

[30] F. De Cola, A. Pellegrino, C. Glößner, D. Penumadu, N. Petrinic, Effect of Particle Morphology, Compaction, and Confinement on the High Strain Rate Behavior of Sand, Exp Mech, 58 (2018) 223-242.

[31] L. Zhang, D. Townsend, N. Petrinic, A. Pellegrino, Pressure and temperature dependent dynamic flow and failure behavior of PMMA at intermediate strain rates, Int. J. Impact Eng, 158 (2021) 104026.

[32] E. Flores-Johnson, Q. Li, Indentation into polymeric foams, Int J Solids Struct, 47 (2010) 1987-1995.

[33] Q. Li, I. Magkiriadis, J.J. Harrigan, Compressive strain at the onset of densification of cellular solids, Journal of cellular plastics, 42 (2006) 371-392.

[34] M. Goel, D. Mondal, M. Yadav, S. Gupta, Effect of strain rate and relative density on compressive deformation behavior of aluminum cenosphere syntactic foam, Materials Science and Engineering: A, 590 (2014) 406-415.

[35] D. Ghosh, A. Wiest, R.D. Conner, Uniaxial quasistatic and dynamic compressive response of foams made from hollow glass microspheres, Journal of the European Ceramic Society, 36 (2016) 781-789.

[36] V.L. Tagarielli, V.S. Deshpande, N.A. Fleck, The high strain rate response of PVC foams and end-grain balsa wood, Composites Part B: Engineering, 39 (2008) 83-91.

[37] N. Gupta, E. Woldesenbet, Compressive fracture features of syntactic foams-microscopic examination, Journal of Materials Science, 37 (2002) 3199-3209.

[38] B. Song, W. Chen, T. Yanagita, D.J. Frew, Temperature effects on dynamic compressive behavior of an epoxy syntactic foam, Composite Structures, 67 (2005) 289-298.

[39] N. Gupta, E. Woldesenbet, S. Sankaran, Studies on compressive failure features in syntactic foam material, Journal of Materials Science, 36 (2001) 4485-4491.

[40] Q. Liu, G. Subhash, A phenomenological constitutive model for foams under

large deformations, Polymer Engineering & Science, 44 (2004) 463-473.

[41] S. Hu, W. Wang, Y. Pan, J. Zhou, Y. Li, Strain rate effect on the properties of foam materials, Explosion and Shock Waves, 23 (2003) 13-18.

[42] N. Gupta, V.C. Shunmugasamy, High strain rate compressive response of syntactic foams: Trends in mechanical properties and failure mechanisms, Materials Science and Engineering: A, 528 (2011) 7596-7605.